HHS Public Access

Author manuscript

Magn Reson Med. Author manuscript; available in PMC 2019 January 22.

Published in final edited form as:

Magn Reson Med. 2016 August ; 76(2): 702–712. doi:10.1002/mrm.25903.

An MRI-Compatible Platform for One-Dimensional Motion Management Studies in MRI

Joris Nofiele[#1], **Qing Yuan**[#1], **Mohammad Kazem**[2], **Ken Tatebe**[1], **Quinn Torres**[1], **Amit Sawant**[1,3], **Ivan Pedrosa**[1,4], and **Rajiv Chopra**[1,2,4,*]

[1]Department of Radiology, University of Texas Southwestern Medical Center, Dallas, Texas, USA.

[2]Sunnybrook Research Institute, Toronto, Ontario, Canada.

[3]Department of Radiation Oncology, University of Texas Southwestern Medical Center, Dallas, Texas, USA.

[4]Advanced Imaging Research Center, University of Texas Southwestern Medical Center, Dallas, Texas, USA.

[#] These authors contributed equally to this work.

Abstract

Purpose: Abdominal MRI remains challenging because of respiratory motion. Motion compensation strategies are difficult to compare clinically because of the variability across human subjects. The goal of this study was to evaluate a programmable system for one-dimensional motion management MRI research.

Methods: A system comprised of a programmable motorized linear stage and computer was assembled and tested in the MRI environment. Tests of the mutual interference between the platform and a whole-body MRI were performed. Organ trajectories generated from a high-temporal resolution scan of a healthy volunteer were used in phantom tests to evaluate the effects of motion on image quality and quantitative MRI measurements.

Results: No interference between the motion platform and the MRI was observed, and reliable motion could be produced across a wide range of imaging conditions. Motion-related artifacts commensurate with motion amplitude, frequency, and waveform were observed. T2 measurement of a kidney lesion in an abdominal phantom showed that its value decreased by 67% with physiologic motion, but could be partially recovered with navigator-based motion-compensation.

Conclusion: The motion platform can produce reliable linear motion within a whole-body MRI. The system can serve as a foundation for a research platform to investigate and develop motion management approaches for MRI.

Keywords

motion; abdominal MRI; respiratory motion; breathing; T2

[*]Correspondence to: Rajiv Chopra, Ph.D., 5323 Harry Hines Boulevard, Dallas, TX 75390-9061. rajiv.chopra@utsuthwestern.edu.

SUPPORTING INFORMATION

Additional Supporting Information may be found in the online version of this article.

INTRODUCTION

Respiratory motion is the main challenge in MRI acquisitions of the abdomen. Motion of the intra-abdominal organs as well as the abdominal wall results in image artifacts such as blurring, aliasing, and ghosting. These artifacts lead to reduced conspicuity of pathology on MRI images, thus compromising its diagnostic performance. For this reason, breath-hold acquisitions are routinely used in clinical practice to achieve motion-free MRI of the torso. Unfortunately, breath-hold approaches may be incompatible with long MRI acquisitions or even short MRI acquisitions in patients with limited breathhold capability. Motion-related artifacts have fueled the development of strategies to reduce or compensate for the effects of respiratory motion during MRI acquisitions of the chest, the abdomen, and to a lesser extent, the pelvis. Examples include averaging of multiple acquisitions, respiratory triggering, and sorting (1,2) through the use of abdominal bellows, pencil beam navigator triggering (3–6), prospective (7) and retrospective (8–12) motion correction, and alternative acquisition strategies such as periodically rotating “blades” in k-space (13,14). However, these strategies are time consuming and are frequently inefficient at eliminating respiratory artifacts entirely. Moreover, different motion compensation strategies may be more applicable to specific image acquisitions and clinical indications.

In addition to the impact on image quality, motion artifacts may have an effect on quantitative MRI measures (eg, longitudinal relaxation time T1, transverse relaxation time T2, effective transverse relaxation rate T2*, apparent diffusion coefficient). Although the effect of motion on image quality has been reported extensively in the literature, its impact on quantitative acquisitions of the torso is lacking. This is undoubtedly due to the difficulty in assessing the impact of motion systematically in human subjects; reproducing the same respiratory motion over minutes when attempting different acquisition strategies in volunteers or patients is virtually impossible. Studies of respiratory patterns in healthy human subjects under well-controlled conditions indicate a coefficient of variation between 10% and 17% for important variables such as respiratory frequency and tidal volumes, which translates into motion artifacts on MR images (15,16).

Addressing abdominal motion is also crucial in the field of image-guided therapeutics, where the goal is to achieve precise therapy delivery to a target volume, while reducing unwanted exposure to normal and/or sensitive tissue structures. This is especially important for noninvasive energy-based therapies such as radiotherapy or high-intensity focused ultrasound energy, which often involve delivery of cytotoxic amounts of energy to moving anatomical targets. For such sites (eg, lung, liver, kidney, pancreas), adaptive energy delivery approaches that track or are triggered by the motion of the target are appropriate (17–19). There is a concerted effort to use real-time imaging to track the motion of target anatomy and to guide adaptive therapy delivery (20). MRI is attractive because it is nonionizing and can be acquired over large fields of view in close to real time (21). Furthermore, emerging therapies such as MRIguided high-intensity focused ultrasound (MR-HIFU) and MRI-guided radiation therapy offer the potential to incorporate real-time MRI during therapy delivery.

A motion platform that can reproducibly replicate the motion of abdominal organs in the MRI environment, combined with a variety of phantoms, would provide the means for developing and testing different diagnostic and therapeutic MRI strategies for specific clinical scenarios and needs. The requirements for such a platform are the ability to move an object within the range encountered for abdominal organ motion (up to 5 cm in the head–foot direction and 3 cm in the anterior–posterior direction) (22), to accommodate a variety of phantoms up to the size of a torso, to operate within the bore of an MRI under any imaging condition, and to deliver periodic, random, and also physiologic motion trajectories. In addition to these properties, the system should not interfere with the energy propagation characteristics of ionizing radiation or ultrasound if used in conjunction with these image-guided therapies.

Previous studies in this area have reported on a range of approaches for producing controlled motion in the MRI using the patient table of the magnet (23), pneumatic systems (24), hydraulic systems (25), electromagnetic systems (26), and piezoceramic actuators (27,28). Many of these developments have occurred for purposes outside of motion management studies such as MR elastography (26,29), MR-HIFU (30), and MRI-guided robotics (31). Recently, commercial systems for motion management studies have been produced (32–34), but these early systems do not meet all of the requirements listed above. In fact, no system to date has been developed specifically as a platform for motion management studies in the MRI for both diagnostic and image-guided therapy research.

In this study, we report on a novel platform for conducting one-dimensional motion management research in the MRI environment. The system construction is described, along with the tests conducted to evaluate its performance and overlap with the requirements stated above. Select examples of how the system could be used to evaluate the effects of periodic harmonic and physiologic motion for imaging studies are given.

METHODS

MRI-Compatible Motion Platform

The motion platform is composed of two parts: a motorized linear stage located inside the bore of the MRI, and driving electronics located at the operator suite. The motorized stage was constructed using three nonmagnetic linear bearing slides and was driven with two nonmagnetic piezoceramic motors (HR4; Nanomotion, Yokneam, Israel). An optical encoder (LIA20; Numerik Jena, Jena, Germany) was used to provide position information. The resulting structure consisted of a large flat surface that could be translated in a linear fashion along one direction. A 3D rendering of the stage is shown in Figure 1. The motor and encoder cables were passed into the room through a filtered enclosure attached to the penetration panel. Details regarding the construction, design, and operation of the motion platform can be found in the Supporting Information. The cables were connected to driving electronics that housed a motor amplifier (AB2; Nanomotion), a power supply, and a connector box to route motion signals to a PCI-based motor controller (PCI7354; National Instruments, Austin, Texas, USA) located on the PC. Customwritten software in LabVIEW (National Instruments) was used to control the motion of the stage along sinusoidal, harmonic, random, or user-defined trajectories. A software manual describing these modes

can be found in the Supporting Information, and the software is freely available from the authors. The software was capable of displaying and recording real-time position of the stage during imaging. Furthermore, a library of physiological motion trajectories was stored in the software for testing with specific imaging sequences. In an MRI experiment, an abdominal phantom with simulated organs, ribs, and subcutaneous fat (Model 057A; CIRS, Norfolk, Virginia, USA), was positioned and secured on top of the motorized stage and was translated along the direction of the bore during imaging to simulate organ motion. A spacer ring was used to suspend a clinical torso coil above the motorized stage so the abdominal phantom could be moved without interference to simulate organ motion during imaging. A photograph of the entire setup on a clinical MRI system is shown in Figure 1.

Characterization of Organ Motion In Vivo

An initial set of measurements was performed in one healthy subject in order to characterize abdominal organ motion in the head–foot direction. The imaging was performed under a protocol approved by the Institutional Review Board at University of Texas Southwestern Medical Center, and informed consent was obtained from the subject. A whole-body 3T MRI scanner (Ingenia; Philips Healthcare, Best, Netherlands) with a dStream anterior–posterior coil (32-channel phased array) was used to image the abdomen of the subject in the supine position. Coronal images were acquired during free-breathing using a high temporal resolution k-t BLAST sequence (repetition time/echo time [TR/TE] = 2.5/1.3 ms; temporal resolution = 0.17 s per image; total scan time = 113 s; field of view [FOV] = 400 × 400 mm^2; voxel size = 2 × 2 mm^2; slice thickness = 10 mm; number of slices = 1), which provided full FOV images of the torso with a spatial and temporal resolution sufficient to assess the motion of the organs in the head–foot direction. Off-line analysis was performed in MATLAB (version 8.3; MathWorks, Natick, Massachusetts, USA) to characterize the displacement of individual organs over time. To obtain organ motion trajectories, a portion of the top edge of each target organ (left/right kidney, liver, or spleen) was selected and used for subsequent automatic detection. The signal intensity at the interface between organs and background was identified by automatic thresholding, and the k-t BLAST images were then converted to binary images. After taking into account the reconstructed image voxel size, the position of the organ interface was directly converted to location in centimeters at different time points. Furthermore, the exact time of acquisition of each dynamic was used to construct the appropriate time series of organ location, thereby reconstructing real organ motion trajectories. High-frequency components of these trajectories due to thresholding and binary conversion were removed through low-pass filtering in the frequency domain. A cutoff frequency of 0.5 Hz was found suitable to remove high-frequency artifacts while preserving the underlying organ motion. Finally, to satisfy the temporal requirements of the motion software, the organ trajectories were up-sampled by a factor of 9 to 20 ms/time point using linear interpolation. The motion trajectories have been provided as text files of position versus time in the Supporting Information.

Performance Characterization

Two tests of the motion platform were conducted in the MRI environment to ensure that there was no significant mutual interaction between the system and the MR scanner. The first test was to evaluate whether the magnetic field and imaging sequences affect the

performance of the motion system. The kidney trajectory extracted from the volunteer scan was replayed by the stage with the phantom attached to it. The position of the stage during motion was tracked by the optical encoder. This test was initially performed with the stage on the MRI table but outside the bore (baseline condition). The stage was then placed at the isocenter inside the bore of the MRI scanner. The same test was repeated with no scanning, as well as under different imaging conditions such as scanning with a high SAR fast spin echo pulse sequence (TR/TE = 1250/80 ms; turbo spin echo factor = 100; acquisition voxel = 0.75 × 0.75 mm^2; slice thickness = 4 mm; FOV = 248 × 200 mm^2; number of slices = 150; acquisition time = 50 s), and with a single-shot spin-echo echoplanar diffusion weighted sequence requiring strong gradients (TR/TE = 982/67 ms; acquisition voxel = 1.6 × 1.6 mm^2; slice thickness = 5 mm; FOV = 120 × 118 mm^2; acquisition time = 3 min, 59 s). The motion trajectories of the stage were compared across all four situations. The second test evaluated whether the motion platform produced any radiofrequency (RF) emissions that might interfere with imaging. A spurious noise test was performed in which the transmitting and receiving body coil swept a range of frequencies from 127.36 to 128.04 MHz (the center frequency of the scanner was 127.74 MHz) to detect any noise frequencies potentially generated by the motion platform. During the test, the stage was operated at the isocenter of the bore, moving with a 3 cm peak-to-peak amplitude sinusoidal motion across a range of frequencies (20, 15, 10, and 5 cycles/min), as well as a random mode of motion where frequency and amplitude changed after every cycle. The noise test was also repeated with the platform turned on and off.

Reproducibility of Motion Artifacts

The ability to generate reproducible imaging artifacts with the platform was evaluated to establish the use of the system for imaging studies performed across different sequences and/or scanners. The first test involved acquiring three separate axial images of the phantom (TE = 20 ms) with the same T2-weighted multishot fast spin echo sequence (TR/TE = 1000/20, 40, 60, 80, 100 ms; acquisition voxel = 1.2 × 1.5 mm^2; slice thickness = 4 mm; FOV = 252 × 201 mm^2; acquisition time = 136 s) while it was in the bore of the magnet, applying the same motion trajectory (2 cm peak-to-peak sinusoidal motion and 15 cycles/min) for each acquisition. The beginning of the motion and of the acquisition were manually synchronized. The mean and coefficient of variance for the three acquired images were evaluated. The second test was similar to the first test except that in between acquisitions, the platform and phantom were brought out of the scanner and a new landmark was assigned. The imaging and motion parameters remained unchanged. Once sent back into the bore of the magnet, a new patient examination was set up, planning images were acquired, and an axial image was prescribed at the same location in the phantom to the best of the operator's ability. The mean and coefficient of variation for three separate image acquisitions were evaluated.

Impact of Motion Amplitude on Image Quality

The motion motorized stage and abdominal phantom were set up in the scanner as shown in Figure 1. Sinusoidal motion of the phantom in the direction of main magnetic field (ie, head–foot direction) was programmed at a frequency of 15 cycles/min, with peak-to-peak amplitudes of 0, 5, 10, 20, and 30 mm. The trajectory extracted from kidney motion in the

volunteer was also used for comparison. To evaluate the effect of through-plane linear motion, axial T2-weighted multishot fast spin echo images (TR/TE = 1000/20, 40, 60, 80, 100 ms; acquisition voxel = 1.2 × 1.5 mm^2; slice thickness = 4 mm; FOV = 252 × 201 mm^2; acquisition time = 136 s) were acquired such that the imaging slices depicted two kidneys, one of which contained a simulated renal lesion. The signal intensities within regions of interest (ROIs) in the kidney (renal parenchyma), background (within abdominal cavity), and lesion were then measured to evaluate the quantitative impact of motion on the measured signal intensity values. The ROIs in the renal parenchyma, the background, and the lesion were 20 × 6 mm^2, 141 × 47 mm^2, and 5 × 6 mm^2, respectively. The same MRI acquisition was performed through the phantom in the coronal plane to assess the in-plane motion and a similar ROI analysis was performed.

Adjustment of Motion Artifact Ghost Spacing

The spacing of systematic noise (ghosts) in the phase encoding direction of the image is related to the imaging acquisition parameters and the characteristics of the underlying motion. According to Haacke and Patrick (35), for two-dimensional (2D) Fourier transform MRI, the spacing of ghosts for periodic through-plane motion can be expressed as

$$\Delta y = m * f * TR * FOV_Y, \quad [3]$$

where Δy is the spacing of artifacts in the y (or phase encode) direction, m represents the specific ghost shifted from true position, f is the frequency of motion (cycles/s), TR is the repetition time (s), and FOV_y is the FOV in the y (or phase encode) direction (mm). Thus, with the ability to control the frequency of motion with the platform, it should be possible to create a range of ghost spacing in MR images. To test this, the motion platform was driven in a sinusoidal fashion (20 mm peak-to-peak amplitude) with the frequency of motion ranging from 0.12 to 0.5 cycles/s (7–30 cycles/min). For each motion trajectory, an axial image (TE = 20 ms) was acquired through the phantom with a T2-weighted multishot fast spin echo sequence (TR/TE = 1000/20, 40, 60, 80, 100 ms; voxel size = 1.2 × 1.5 mm^2; slice thickness = 4 mm; FOV = 252 × 201 mm^2; acquisition time = 136 s) and the spacing between ghosts was measured in MATLAB. The spacing of ghosts was measured at three locations where a strong interface was present, and the standard deviation of the measurement was also calculated to assess variability in measurement. The relationship between the measured and predicted ghosts was compared. Additionally, one acquisition was performed where the frequency was 1 cycle/s, which matched the repetition time of the acquisition sequence.

Evaluation of Motion-Compensation Strategies

As an example of how this motion platform could be used for characterization of impact of motion on quantitative MRI, a T2 map of the phantom was calculated under different motion conditions. MRI of the phantom was performed in a coronal plane, in which both kidneys, embedded kidney lesion, and liver were visible, using a multishot fast spin echo sequence (TR/TE = 1000/20, 40, 60, 80, 100 ms; acquisition voxel = 1.2 × 1.5 mm^2; slice thickness = 4 mm; slice gap = 4 mm; FOV = 200 × 300 mm^2; acquisition time = 202 s). A T2 map was

generated from this scan on a scanner. Circular ROIs were drawn manually on the T2 maps obtained with no motion to calculate the mean T2 values for the kidney, the liver, and the lesion using the kidney motion trajectory with navigator triggering. Precision of measurement was calculated as standard deviation of T2 divided by the average T2 in the region of interest. Motion compensation was performed using MotionTrak (Ingenia; Philips Healthcare), a navigator triggering technique developed for a clinical setting to compensate for respiratory motion during cardiac and abdominal imaging. For clinical imaging, a pencil beam navigator is usually placed at the level of the diaphragm where the lung/liver interface provides a good contrast. In this study, the gating window was positioned at the inferior edge of the phantom, with half of the window in air and the other half in the phantom to ensure the interface remained within the navigator window (gating window length = 60 mm; trigger delay = 0 ms; number of beams = 1) throughout imaging.

RESULTS

MRI-Compatible Motion Platform

The performance of the motion platform was measured and tabulated (Supporting Table S1). The total range of motion of the stage was 138 mm, which is beyond the maximum range of head–foot motion for abdominal organs in a typical human subject (36). The maximum velocity of the stage was measured to be 47.7 cm/s when unloaded and 38.1 cm/s when loaded with a 5.4 kg phantom. The acceleration under the same conditions was 445 and 286 cm/s^2, respectively. These values were obtained with a specific set of tuning parameters which are customizable for other applications. The existing commercial systems for linear motion in the MRI typically have a range of approximately 5 cm and an accuracy of 0.1 mm. However, they tend to be limited in their maximum velocity and lack full programmability of motion trajectories. To illustrate, an empirical measurement was performed to determine the fastest time possible for the stage to perform one cycle of forward movement (7.6 cm) and immediate reverse movement of the same distance, and found to be 0.8 ± 0.05 s, with an average speed of 19 cm/s. The velocity and acceleration limits also met the requirements to simulate a wide range of organ trajectories under normal and abnormal breathing conditions. The precision of motion for the stage was ± 0.013 mm for low speeds, and approximately ± 0.1 mm for high-speed motion. This is equivalent to <5% of a 2-mm-thick imaging slice in the worstcase scenario. All of these measured specifications were the same inside and outside the MR scanner. For userdefined trajectories, the software sampled the motion at 20 ms intervals and could replay up to 10 min of arbitrary motion, based on memory limitations of the motor controller. After this time, the motion trajectory was repeated.

Characterization of Organ Motion

Figure 2 shows a coronal image from the k-t BLAST imaging time series acquired in the volunteer. The liver, spleen, and two kidneys are well visualized in this image. Using the organ tracking method described earlier, the displacement of each organ in the head–foot direction was obtained (Fig. 2B). The amplitudes of motion varied significantly over time, and across organs, emphasizing the importance of creating organ-specific trajectories. These trajectories were sampled and stored as digital files for the motion platform to replay in subsequent measurements.

Performance Characterization

Figure 3A shows a 30-s measurement of the displacement of the stage while performing a kidney trajectory under different conditions. As the figure shows, the movement of the stage was unaffected by the magnetic field of the scanner or by RF or gradient activities during scanning. These results demonstrate the ability of the system to reliably deliver a desired trajectory in the MR scanner under a wide range of imaging conditions. Figure 3B shows the results of the noise scan performed on the scanner. Three peaks can be seen in the figure, one of which is due to the water signal of the phantom at the Larmor frequency. The other two peaks were always present for all motion tests, and only disappeared when the control electronics for the platform were turned off. This points to the source arising from RF emissions from some of the electronics components associated with the motor or power supplies. However, these peaks fall well outside the typical bandwidth of MRI sequences (gray region in Fig. 3B) and will therefore not introduce artifacts while the system is in operation. Outside of these two isolated peaks, the baseline intensity of the frequency spectrum was unchanged regardless of whether the stage was in operation. Furthermore, the noise spectrum shown in Figure 3B was unchanged regardless of the motion trajectory performed by the platform.

Reproducibility of Motion Artifacts

The results of the two reproducibility tests are shown in Figure 4. The test of repeatability with the phantom left as the same position (top row) showed a very good alignment when the average of three acquisitions was calculated (left image). The average coefficient of variance across the image was only 4%, indicating a high degree of repeatability. The second test, involving re-landmarking of the phantom and a new patient setup, also showed an average image with little blurring (ie, few misaligned ghosts). The average coefficient of variance increased to 17%, indicating a higher degree of variance compared with the first repeatability test, as expected.

Impact of Motion Amplitude on Image Quality

Figure 5 shows axial T2-weighted images through the phantom under different motion conditions. Compared with images acquired without motion, the increase in ghosting artifacts in the phase-encode direction is apparent with increasing motion amplitude. At 5-mm peak-to-peak sinusoidal motion (approximately equivalent to the slice thickness), there was minimal effect on the image quality beyond a few discrete ghosting artifacts. At 20-mm displacement and beyond, artifacts included stronger ghosting as well as slice misregistration from outside the imaging plane. Image degradation became severe at 30 mm of displacement (approximately seven times the slice thickness). The physiologic pattern of kidney motion produced a different type of artifact compared with the sinusoidal trajectories due to the time varying amplitude and frequency of the motion. Figure 6 shows the standard deviation and the lesion-to-background ratio of the signal intensity in selected regions of interest for the different motion amplitudes, and for the simulated physiologic motion trajectory. Similar results were found for the impact of motion on image quality on the coronal acquisition, which can be seen in Figure 7.

Adjustment of Motion Artifact Ghost Spacing

The relationship between image ghost spacing and the frequency of periodic motion is given in Figure 8. A linear relationship can be observed for periodic motion ranging from 7 to 30 cycles/min. Furthermore, the measured ghost spacing was in excellent agreement with the predictions from the relationship given in Equation 1. Finally, when the period of motion was set equal to the repetition time of the imaging sequence, no ghosts were observed. These results highlight the ability to control and adjust the types of motion artifacts produced in MRI using the motion platform.

Evaluation of Motion Compensation Strategies

Figures 9 and 10 show the impact of motion on T2 quantification in the phantom. For the stationary phantom, the T2 values of the liver, kidney, and renal lesion were calculated with a precision of 3.3%, 2.4%, and 28.5%, respectively. Once physiologic kidney motion was incorporated into the phantom during the T2 mapping sequence, the contrast between these structures quickly diminished, making it difficult to identify the lesion. Furthermore, the estimated T2 value of the lesion decreased to approximately a quarter of its original value, from 1216 to 319 ms. The same image acquisition using navigator trigger improved the image quality significantly, restoring the contrast between kidney parenchyma and the lesion, and recovering the T2 value by 50%. For liver and kidney, T2 values elevated due to the image artifact under motion. With navigator trigger, T2 values returned to the ones without motion.

DISCUSSION

This study presents a novel platform for motion management research in MRI. The proposed system is MRI compatible and can operate in the bore of a whole-body MRI during scanning using a wide range of sequences and motion trajectories with no detectable interference on the acquired images. Furthermore, the process of MRI shows no measurable effect on the performance of the motion platform when compared with its performance outside the magnet environment. The design of the stage in this study was a flat surface that could be moved in a linear fashion, which was suitable for loading it with a torso-sized phantom. The stage is capable of moving a load of at least 5.4 kg with little impact on its performance, and the range of motion, maximum velocity and acceleration, and precision of motion were all well within the values measured in the cranial–caudal direction for abdominal organs in human subjects. When successive imaging measurements were made with the phantom, very repeatable ghosting patterns were observed in the acquired images. These characteristics could make this platform a valuable research platform for the development and evaluation of imaging strategies for motion compensation.

Another valuable aspect of the motion platform was the ability to program custom motion trajectories using the software interface associated with the system. In this study, the displacement over time for multiple abdominal organs was measured using a real-time MRI sequence in a healthy volunteer. The trajectories were then used to recreate organ motion using the phantom and platform. With this feature, a library can be built consisting of cranial–caudal motion trajectories including patients with respiratory difficulty, coughs,

pauses, and other clinically relevant scenarios. The ability to test sequences with all of these different conditions would greatly assist in determining the suitability of different acquisition and motion compensation strategies for specific clinical situations.

From the preliminary studies performed with the platform, the change in the lesion-to-background tissue ratio and the standard deviation of signal in an organ could be measured for different amplitudes of motion to understand the relationship between these variables. In addition, the difference between sinusoidal and physiologic motion was evident, which emphasized the importance of using realistic trajectories obtained from human subjects. These experiments provide the basis for assessing different acquisition and motion compensation strategies in clinical MRI protocols for torso imaging and the opportunity to select those that are more robust to motion-related artifacts. Finally, the impact of motion on a conventional multiecho T2 mapping sequence was evident, reducing the measured T2 value by over a factor of 3 in the presence of motion. Using navigator motion compensation the T2 value was recovered partially, but not completely to its original value measured without motion. Similar studies could be performed to evaluate the impact of motion on other clinically relevant quantitative MRI parameters.

A main limitation of the proposed platform is the restriction of motion to one linear dimension. Abdominal organ motion occurs primarily in the cranial–caudal direction, with some components in the dorsal–ventral and right–left direction. Additional axes could be built to produce motion in these additional directions and are currently being planned. However, this still limits the platform to the study of rigid body motion. Abdominal organs deform and change shape during motion, and nonrigid deformation models and correction schemes may have advantages (37,38). In these situations, the motion platform could be used as an actuator to deform a compliant phantom. Another limitation of the platform in its current configuration is potential interference of the materials in the motorized stage with external sources of energy for studies involving high-intensity focused ultrasound or external beam radiation. The metallic stages and motors may change the propagation and scatter of a radiation beam, and the plastic stage precludes delivery of ultrasound from a clinical HIFU system. A short-term solution to this would be to use the stage as an actuator to move a phantom placed on the patient table such that the actual motorized components were not in the path of the beam.

In conclusion, the proposed system meets or exceeds the characteristics of motion in the cranial–caudal direction for abdominal organs with respect to displacement, velocity, and acceleration. Even with the restriction to linear motion, the system can be used to evaluate the effectiveness of clinical motion correction schemes, which are largely based on the assumption that cranial–caudal motion is the predominant contributor to artifacts.

Supplementary Material

Refer to Web version on PubMed Central for supplementary material.

ACKNOWLEDGMENTS

Ivan Pedrosa and Rajiv Chopra contributed equally to the conception and design of the study.

Grant sponsor: Cancer Prevention and Research Initiative of Texas; Grant number: R1308; Grant sponsor: National Institutes of Health; Grant number: 1R01CA154475.

REFERENCES

1. Robson PM, Madhuranthakam AJ, Dai W, Pedrosa I, Rofsky NM, Alsop DC. Strategies for reducing respiratory motion artifacts in renal perfusion imaging with arterial spin labeling Magn Reson Med 2009; 61:1374–1387. [PubMed: 19319891]
2. Zech CJ, Herrmann KA, Huber A, Dietrich O, Stemmer A, Herzog P,Reiser MF, Schoenberg SO. High-resolution MR-imaging of the liver with T2-weighted sequences using integrated parallel imaging: comparison of prospective motion correction and respiratory triggering. J Magn Reson Imaging 2004;20:443–450. [PubMed: 15332252]
3. Wang Y, Rossman PJ, Grimm RC, Wilman AH, Riederer SJ, Ehman RL.3D MR angiography of pulmonary arteries using real-time navigator gating and magnetization preparation. Magn Reson Med 1996;36:579–587. [PubMed: 8892211]
4. Kohler MO, Denis de Senneville B, Quesson B, Moonen CT, Ries M.Spectrally selective pencil-beam navigator for motion compensation of MR-guided high-intensity focused ultrasound therapy of abdominal organs. Magn Reson Med 2011;66:102–111. [PubMed: 21305602]
5. Nehrke K, Bornert P, Groen J, Smink J, Bock JC. On the performanceand accuracy of 2D navigator pulses. Magn Reson Imaging 1999;17: 1173–1181. [PubMed: 10499679]
6. Felmlee JP, Ehman RL, Riederer SJ, Korin HW. Adaptive motion compensation in MRI: accuracy of motion measurement. Magn Reson Med 1991;18:207–213. [PubMed: 2062232]
7. Maclaren J, Herbst M, Speck O, Zaitsev M. Prospective motion correction in brain imaging: a review. Magn Reson Med 2013;69:621–636. [PubMed: 22570274]
8. Vaillant G, Prieto C, Kolbitsch C, Penney G, Schaeffter T. Retrospective rigid motion correction in k-space for segmented radial MRI. IEEE Trans Med Imaging 2013;33:1–10. [PubMed: 23782798]
9. Kochunov P, Lancaster JL, Glahn DC, Purdy D, Laird AR, Gao F, FoxP. Retrospective motion correction protocol for high-resolution anatomical MRI. Hum Brain Mapp 2006;27:957–962. [PubMed: 16628607]
10. Hansen MS, Sorensen TS, Arai AE, Kellman P. Retrospective reconstruction of high temporal resolution cine images from real-time MRI using iterative motion correction. Magn Reson Med 2012;68:741–750. [PubMed: 22190255]
11. Ehman RL, Felmlee JP. Adaptive technique for high-definition MRimaging of moving structures. Radiology 1989;173:255–263. [PubMed: 2781017]
12. Odille F, Cindea N, Mandry D, Pasquier C, Vuissoz PA, Felblinger J.Generalized MRI reconstruction including elastic physiological motion and coil sensitivity encoding. Magn Reson Med 2008;59:1401–1411. [PubMed: 18421689]
13. Pipe JG. Motion correction with PROPELLER MRI: application tohead motion and free-breathing cardiac imaging. Magn Reson Med 1999;42:963–969. [PubMed: 10542356]
14. Deng J, Larson AC. Modified PROPELLER approach for T2-mappingof the abdomen. Magn Reson Med 2009;61:1269–1278. [PubMed: 19353672]
15. Shea SA, Walter J, Murphy K, Guz A. Evidence for individuality of breathing patterns in resting healthy man. Respir Physiol 1987;68:331–344. [PubMed: 3616179]
16. Shea SA, Walter J, Pelley C, Murphy K, Guz A. The effect of visualand auditory stimuli upon resting ventilation in man. Respir Physiol 1987;68:345–357. [PubMed: 3616180]
17. Celicanin Z, Auboiroux V, Bieri O, Petrusca L, Santini F, Viallon M,Scheffler K, Salomir R. Real-time method for motion-compensated MR thermometry and MRgHIFU treatment in abdominal organs. Magn Reson Med 2014;72:1087–1095. [PubMed: 24243500]
18. Pichardo S, Kohler M, Lee J, Hynnyen K. In vivo optimisation studyfor multi-baseline MR-based thermometry in the context of hyperthermia using MR-guided high intensity focused ultrasound for head and neck applications. Int J Hyperthermia 2014;30:579–592. [PubMed: 25430989]
19. Ries M, de Senneville BD, Roujol S, Berber Y, Quesson B, Moonen C.Real-time 3D target tracking in MRI guided focused ultrasound ablations in moving tissues. Magn Reson Med 2010;64:1704–1712. [PubMed: 20878763]

20. Sawant A, Keall P, Pauly KB, Alley M, Vasanawala S, Loo BW, Jr,Hinkle J, Joshi S. Investigating the feasibility of rapid MRI for image-guided motion management in lung cancer radiotherapy. Biomed Res Int 2014;2014:485067. [PubMed: 24524077]
21. Li G, Citrin D, Camphausen K, Mueller B, Burman C, Mychalczak B,Miller RW, Song Y. Advances in 4D medical imaging and 4D radiation therapy. Technol Cancer Res Treat 2008;7:67–81. [PubMed: 18198927]
22. Hallman JL, Mori S, Sharp GC, Lu HM, Hong TS, Chen GT. A fourdimensional computed tomography analysis of multiorgan abdominal motion. Int J Radiat Oncol Biol Phys 2012;83:435–441. [PubMed: 22197238]
23. Riek JK, Tekalp AM, Smith WE, Kwok E. Out-of-plane motion compensation in multislice spin-echo MRI. IEEE Trans Med Imaging 1995;14:464–470. [PubMed: 18215850]
24. Muntener M, Patriciu A, Petrisor D, Mazilu D, Bagga H, Kavoussi L,Cleary K, Stoianovici D. Magnetic resonance imaging compatible robotic system for fully automated brachytherapy seed placement. Urology 2006;68:1313–1317. [PubMed: 17169653]
25. Hynynen K, Freund WR, Cline HE, Chung AH, Watkins RD, Vetro JP,Jolesz FA. A clinical, noninvasive, MR imaging-monitored ultrasound surgery method. Radiographics 1996;16:185–195. [PubMed: 10946699]
26. Muthupillai R, Lomas DJ, Rossman PJ, Greenleaf JF, Manduca A,Ehman RL. Magnetic resonance elastography by direct visualization of propagating acoustic strain waves. Science 1995;269:1854–1857. [PubMed: 7569924]
27. Chinzei K, Miller K. Towards MRI guided surgical manipulator. MedSci Monit 2001;7:153–163.
28. Chopra R, Curiel L, Staruch R, Morrison L, Hynynen K. An MRIcompatible system for focused ultrasound experiments in small animal models. Med Phys 2009;36:1867–1874. [PubMed: 19544806]
29. Chopra R, Arani A, Huang Y, Musquera M, Wachsmuth J, Bronskill M, Plewes D. In vivo MR elastography of the prostate gland using a transurethral actuator. Magn Reson Med 2009;62:665–671. [PubMed: 19572390]
30. Yiallouras C, Damianou C. Review of MRI positioning devices forguiding focused ultrasound systems. Int J Med Robot 2015;11:247–255. [PubMed: 25045075]
31. Elhawary H, Tse ZT, Hamed A, Rea M, Davies BL, Lamperth MU. The case for MR-compatible robotics: a review of the state of the art. Int J Med Robot 2008;4:105–113. [PubMed: 18481822]
32. Modus QA MRI respiratory motion. http://modusmed.com/qaphantoms/mri-respiratory-motion. Accessed April 28, 2015.
33. CIRS MRI-Linac Dynamic Phantom. http://www.cirsinc.com/products/all/112/mri-linac-dynamic-phantom/. Accessed April 28, 2015.
34. MRI-compatible Linear Motion Stage. http://vitalbt.com/products/. Accessed April 28, 2015.
35. Haacke EM, Patrick JL. Reducing motion artifacts in two-dimensionalFourier transform imaging. Magn Reson Imaging 1986;4:359–376. [PubMed: 3669950]
36. Muller A, Petrusca L, Auboiroux V, Valette PJ, Salomir R, Cotton F.Management of respiratory motion in extracorporeal high-intensity focused ultrasound treatment in upper abdominal organs: current status and perspectives. Cardiovasc Intervent Radiol 2013;36:1464–1476. [PubMed: 24178235]
37. Menini A, Slavin GS, Stainsby JA, Ferry P, Felblinger J, Odille F. Motion correction of multi-contrast images applied to T(1)and T(2)quantification in cardiac MRI. MAGMA 2015;28:1–12.
38. Xue H, Guehring J, Srinivasan L, Zuehlsdorff S, Saddi K, Chefdhotel C, Hajnal JV, Rueckert D. Evaluation of rigid and non-rigid motion compensation of cardiac perfusion MRI. Med Image Comput Comput Assist Interv 2008;11:35–43.

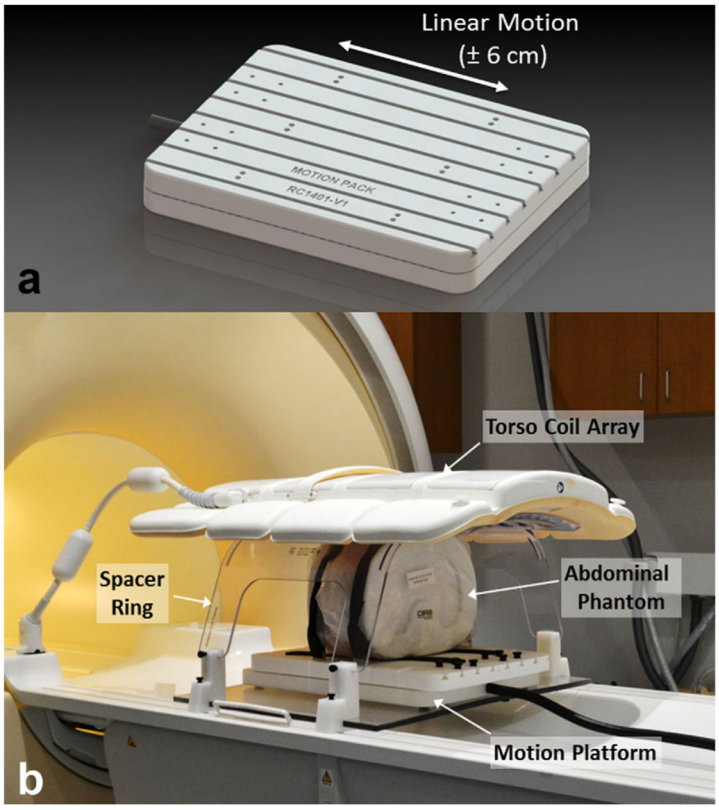

FIG. 1.

(**A**) Rendering of an MRI-compatible motion platform capable of producing linear motion within a clinical MRI scanner. (**B**) Photograph of the setup used for this study. An abdominal phantom was affixed to the motion platform and a clinical torso array was held above it using a spacer ring. The phantom was free to move in the head–foot direction during imaging to simulate abdominal organ motion.

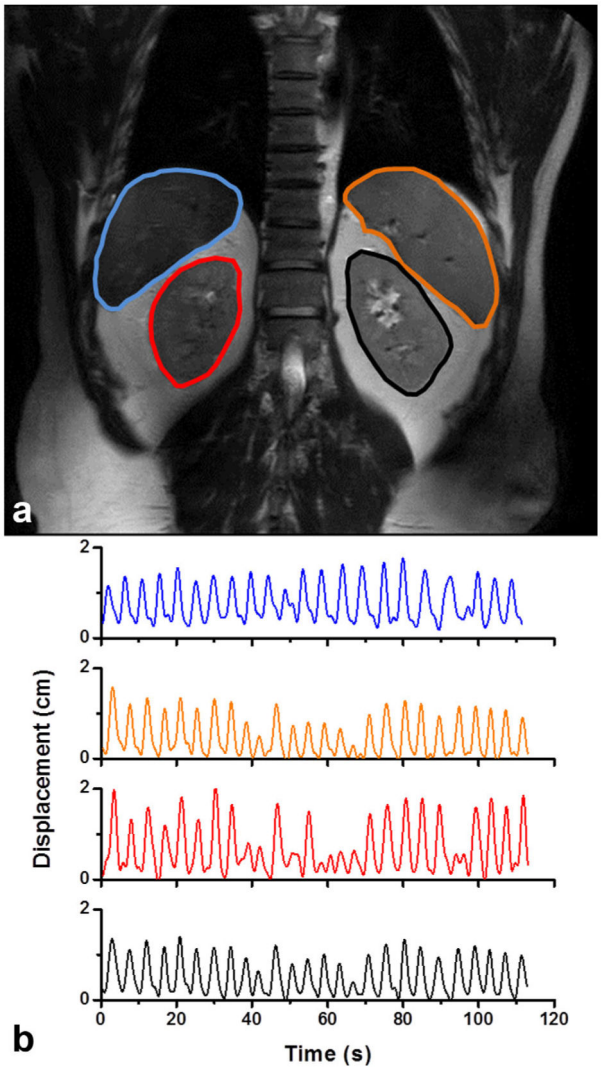

FIG. 2.

(**A**) A single frame from a coronal time series (single slice) acquired in the abdomen of a healthy volunteer was used to track the motion of the liver (blue), spleen (orange), right kidney (red), and left kidney (black) over multiple breathing cycles. (**B**) The displacement in the head–foot direction as a function of time is shown for each organ in the free-breathing volunteer.

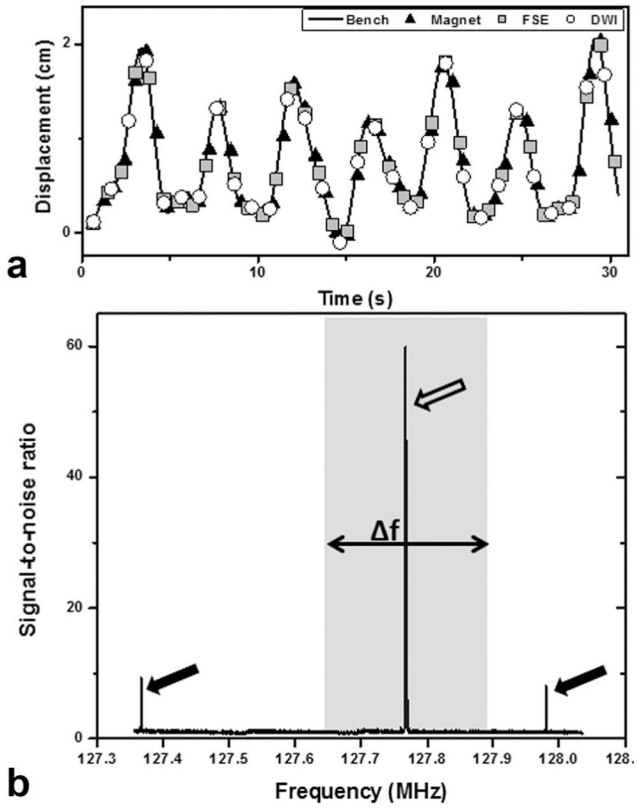

FIG. 3.

(**A**) The displacement versus time of the motion platform during playback of a kidney trajectory. The motion was performed outside the magnet (bench), inside the bore (magnet), during a multislice fast spin echo sequence, and during a single shot diffusion-weighted imaging sequence. The different imaging conditions had negligible impact on the performance of the platform. (**B**) A noise spectrum analysis was performed to evaluate the impact of the motion platform on MRI. Two additional signals (black arrows) outside the imaging bandwidth (gray region) were observed once the electronics for the system were turned on; however, these were significantly lower in amplitude than the water signal. No additional noise peaks were observed across a wide range of motion trajectories. The large peak within the imaging bandwidth (white arrow) was from a water phantom placed on the motion platform.

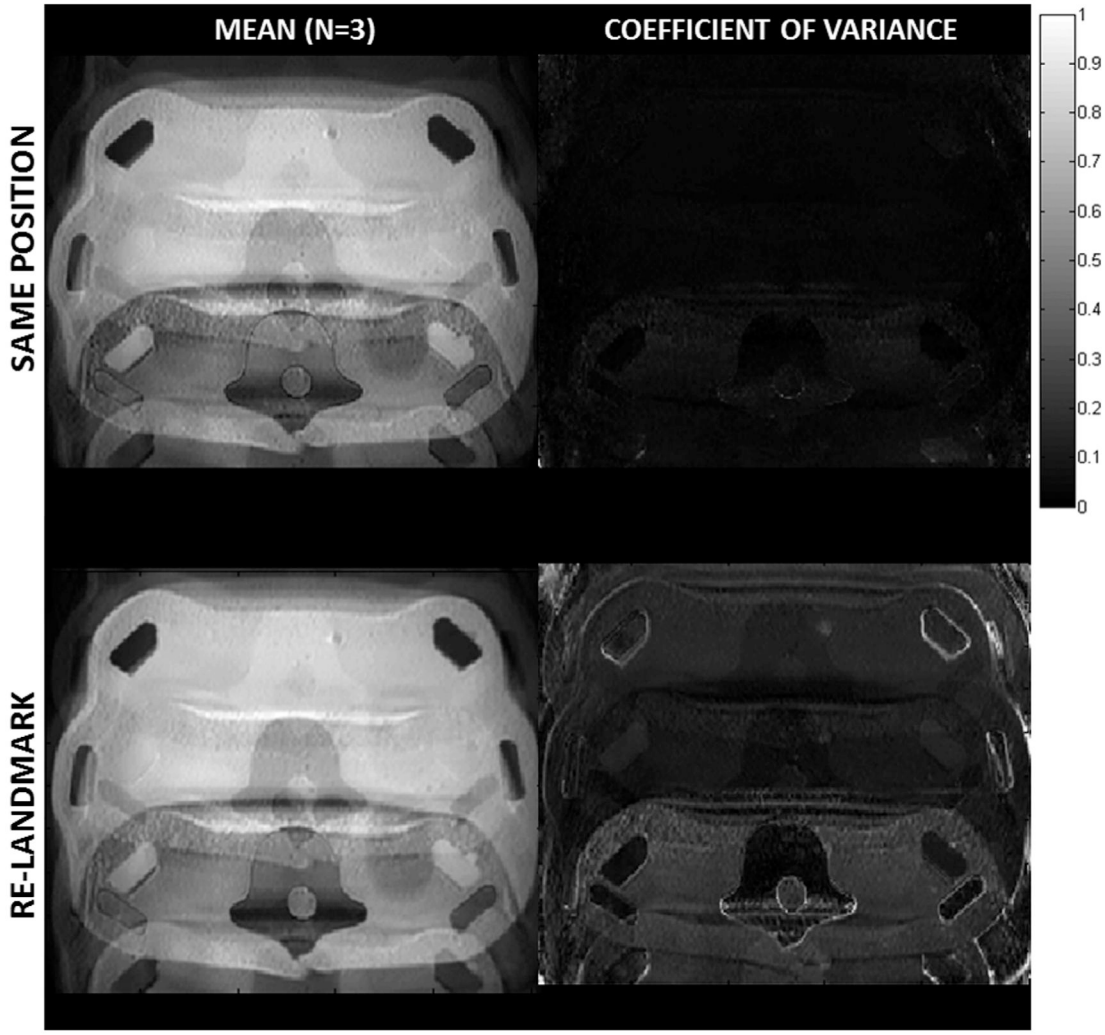

FIG. 4.

The mean (left) and coefficient of variance (right) for repeat imaging of the phantom (n = 3) with a sinusoidal through-plane motion trajectory of 20-mm peak-to-peak (15 cycles/min) for two different conditions. The first case (top row) involved three successive imaging scans with the same motion and position. The second case (bottom row) involved three successive scans with the same motion, but in each case the phantom was brought out of the bore and re-landmarked with the system before being scanned. The coefficient of variance was lower for the first case but remained very good for both cases. The repeatability of the location and spacing of ghosts is excellent for both cases.

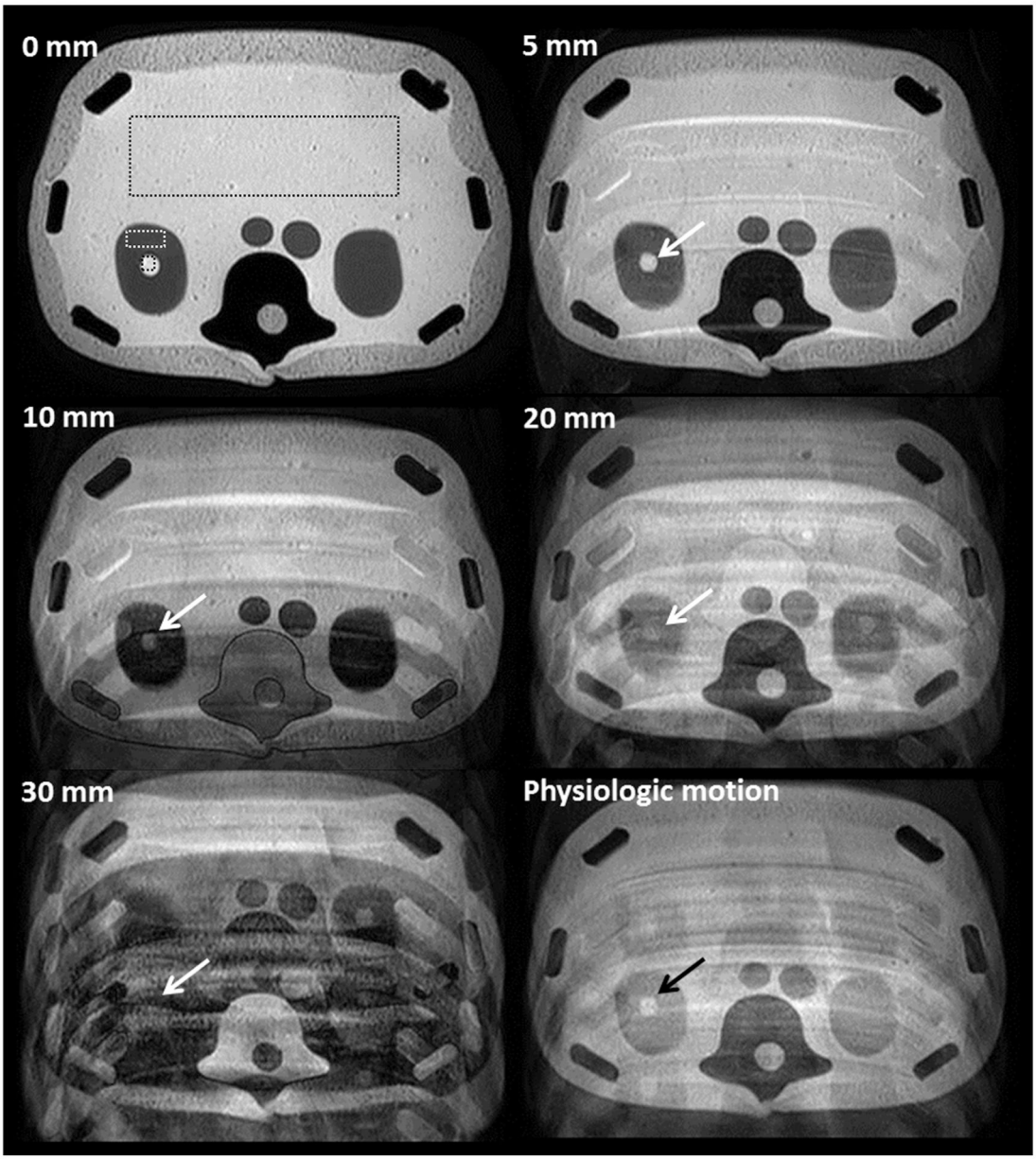

FIG. 5.

A series of axial 2D T2-weighted images (TR/TE = 1000/100 ms; acquisition matrix = 252 × 201; slice thickness = 4 mm) of the anthropomorphic phantom acquired through the kidneys with varying degrees of sinusoidal displacement in the foot–head direction (0–30 mm) or simulated physiologic kidney motion depict the degradation in image quality with motion. The movement was continuous during the entire image acquisition process and occurred at a frequency of 15 cycles/min in the slice direction (z axis, through-plane). Image acquisition time was approximately 2 min. Different ROIs were placed on the center of the phantom, renal parenchyma, and simulated renal lesion in the right kidney to evaluate the change of signal intensity due to motion. Note the decreased conspicuity of the right renal

lesion with increasing degrees of sinusoidal motion (white arrows) and to less extent, with physiologic motion with displacement about 20 mm (black arrow).

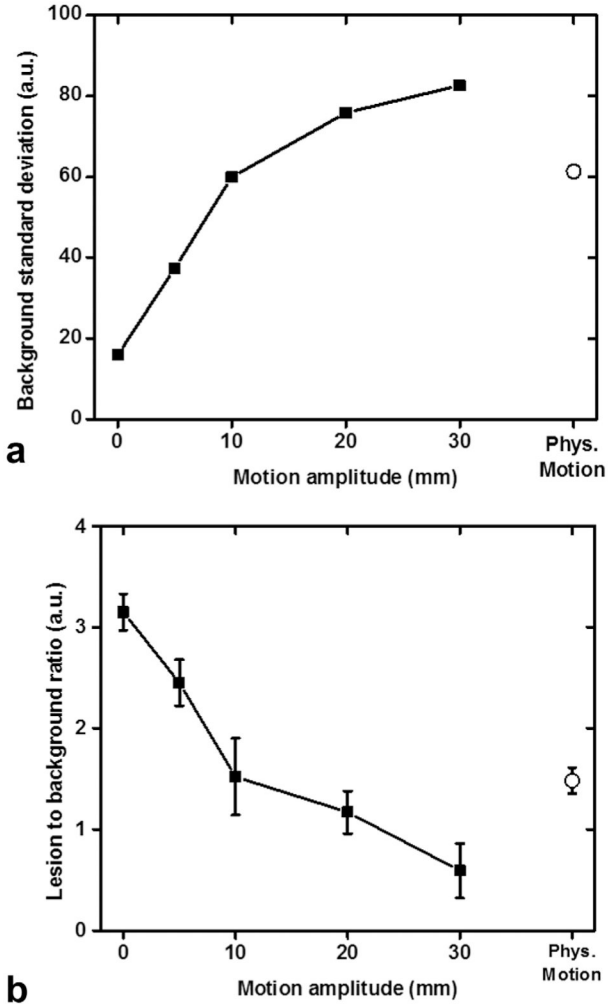

FIG. 6.

Rectangular regions of interest (ROIs) displayed in Figure 4 were copied and pasted on all acquisitions (TE = 100 ms) with different degrees of sinusoidal and physiologic motion for quantitative assessment of image quality and lesion detection. (**A**) Standard deviation of the background signal (large rectangular ROI in the center of the phantom) increases uniformly with sinusoidal motion of increasing amplitude. Physiological motion results in a three-fold increase of the standard deviation of the background. Signal intensities used were obtained from the regions of interest in Figure 5. (**B**) Renal lesion-to-background ratio of signal intensities decreases uniformly with sinusoidal motion of increasing amplitude making the detection of the lesion more difficult. We also observe a two-fold decrease in the lesion-to-background ratio with physiological motion.

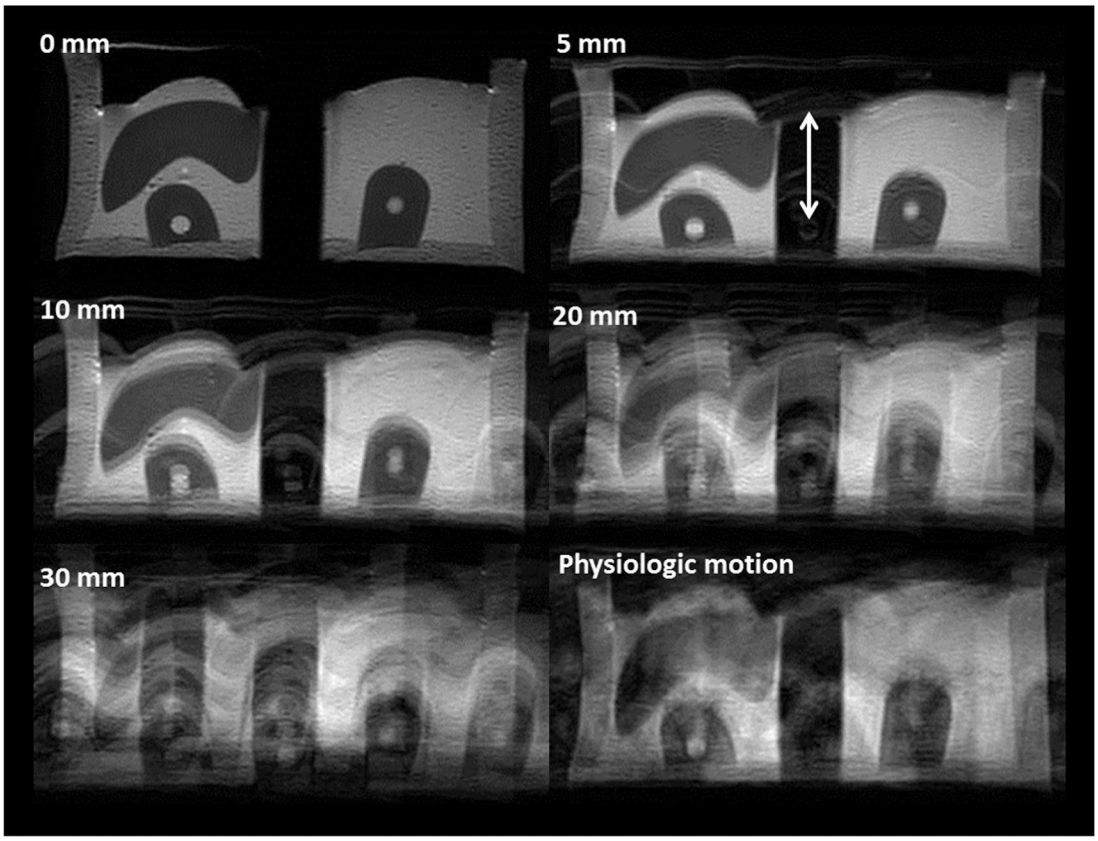

FIG. 7.

A series of coronal images acquired through the phantom with varying degrees of sinusoidal motion (0–30 mm) or simulated physiologic kidney motion in the cranial–caudal direction (z axis, indicated by the arrows). The degradation in image quality with increasing motion amplitude is clear. Movement was continuous during the entire image acquisition process and occurred at a frequency of 15 cycles/min. Image acquisition time was approximately 3 min.

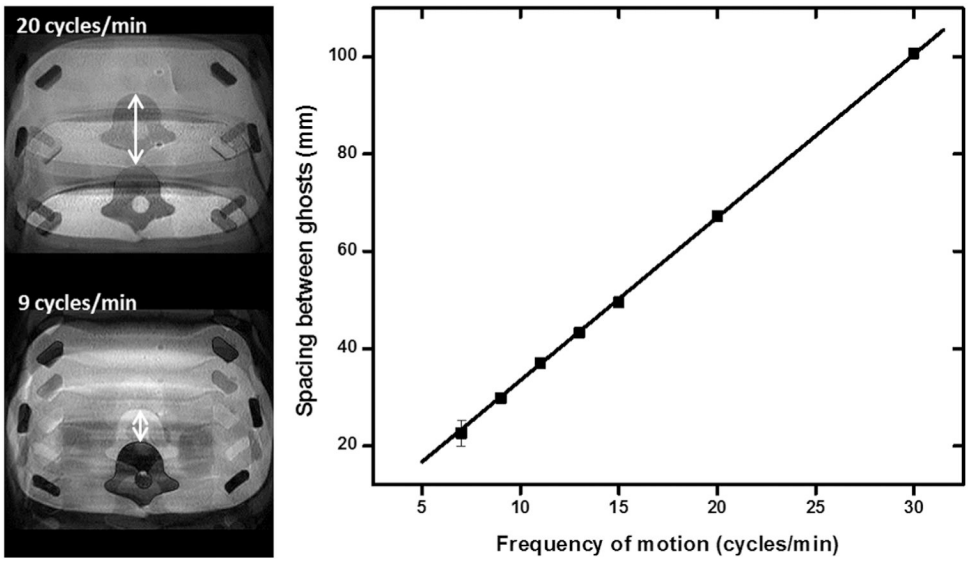

FIG. 8.

The measured and predicted spacing between ghosts for images acquired in the presence of periodic through-plane motion with increasing frequency. A consistent linear increase in ghost spacing was observed, in excellent agreement with the predictions from Haacke and Patrick (35). These results demonstrate the high degree of repeatability and control available with this motion platform.

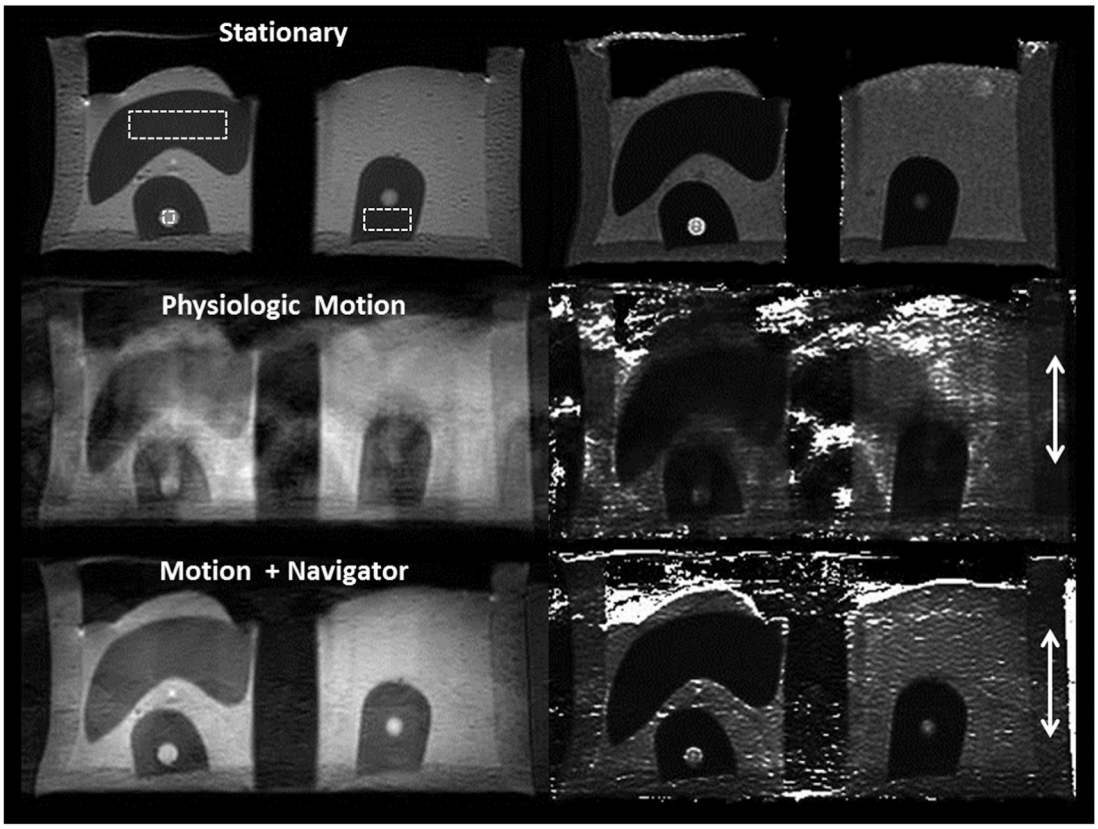

FIG. 9.

A multiecho coronal T2 mapping acquisition (TR = 1000 ms; TE = 20, 40, 60, 80, 100 ms; acquisition matrix = 252 × 200; slice thickness = 4 mm; voxel size = 1.2 × 1.5 mm^2) of the phantom acquired through the kidneys without phantom motion (top), physiologic motion of the phantom in the cranial–caudal (z-axis, arrows) direction (middle), and physiologic motion but using a navigator to trigger acquisition (bottom). The left column shows an image acquired with TE = 100 ms; the right column shows the resulting T2 map calculated from the multiecho series. Large and small dotted-line rectangles were placed on the liver and renal parenchyma, respectively. A dotted-line square was placed on the simulated renal lesion in the right kidney. Note the severe artifacts induced by phantom motion on the T2 map, which are partially corrected with the use of the navigator.

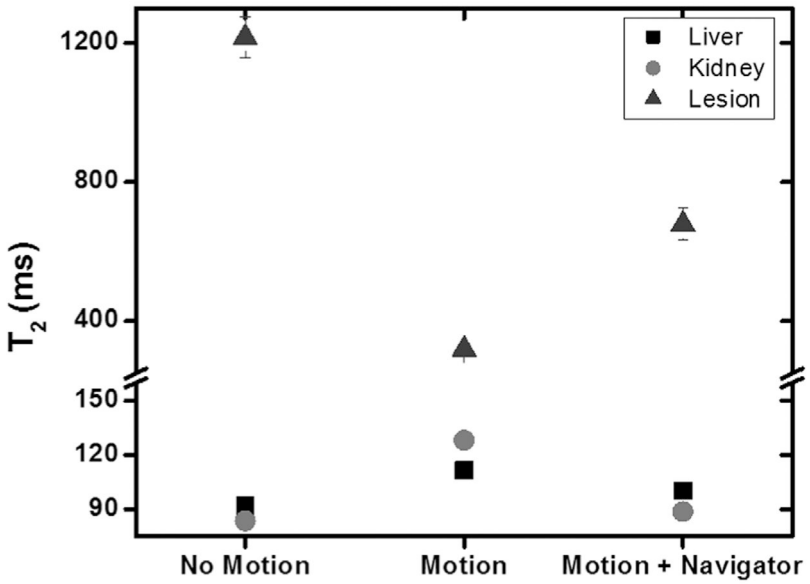

FIG. 10.

T2 values measured in the phantom within the liver, kidney, and simulated renal lesion (regions of interest in Fig. 7). The presence of motion caused a three-fold reduction in the estimate of T2 in the lesion, and an approximately 1.5-fold increase in the T2 of the liver and kidney. When a navigator was used to trigger image acquisition, the T2 estimates in the liver and kidney were much closer to the baseline estimates. This improvement was also present for the simulated renal lesion, although the difference in the calculated T2 compared with the baseline estimate was still substantial.